Multi-frequency shear modulus measurements discriminate tumorous from healthy tissues

Stéphane Nicolle, Jean-François Palierne, David Mitton, Hélène Follet, Cyrille B. Confavreux

Multi-frequency shear modulus measurements discriminate tumorous from healthy tissues

S. Nicolle, J.-F. Palierne, D. Mitton, H. Follet, C.B. Confavreux

PII: S1751-6161(23)00074-7

DOI: https://doi.org/10.1016/j.jmbbm.2023.105721

Reference: JMBBM 105721

To appear in: *Journal of the Mechanical Behavior of Biomedical Materials*

Received Date: 19 July 2022

Revised Date: 7 February 2023

Accepted Date: 8 February 2023

Please cite this article as: Nicolle, S., Palierne, J.-F., Mitton, D., Follet, H., Confavreux, C.B., Multi-frequency shear modulus measurements discriminate tumorous from healthy tissues, *Journal of the Mechanical Behavior of Biomedical Materials* (2023), doi: https://doi.org/10.1016/j.jmbbm.2023.105721.

Mouse samples

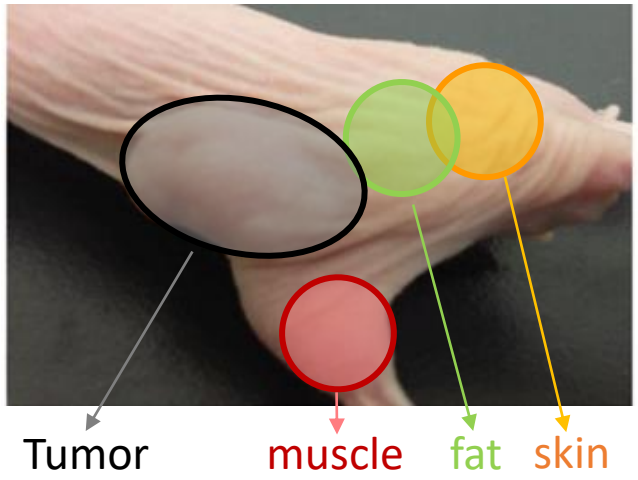

Subcutaneously injected with **human breast cancer** cells

Experiment and Modelling

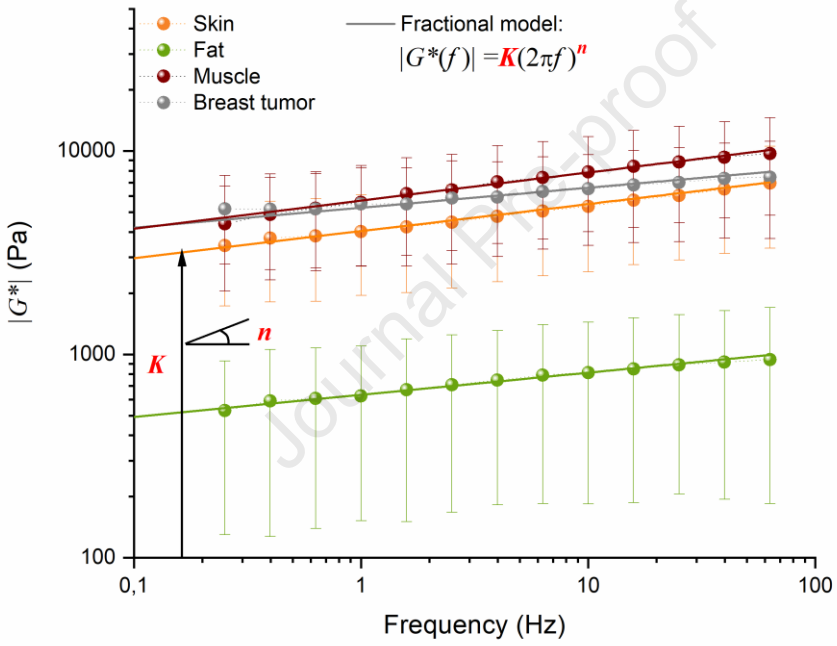

Analysis and Conclusions

Mann-Whitney test	*p-value for* K	*p-value for* n
Fat – Tumor	**0.00025**	0.43
Muscle – Tumor	0.84	**0.00041**
Skin – Tumor	0.14	**0.000019**

Bold: significant difference at level α = 0.05

$$K_{fat} << K_{tumor} \approx K_{muscle} \approx K_{skin}$$

→ Tumors are distinguished from fat by the **modulus magnitude**

$$n_{tumor} \approx n_{fat} < n_{muscle} \approx n_{skin}$$

→ Tumors are distinguished from muscle and skin by the **modulus frequency dependence**

Multi-frequency shear modulus measurements discriminate tumorous from healthy tissues

S. Nicolle[a,*], J.-F. Palierne[b] , D. Mitton[a], H. Follet[c], C. B. Confavreux[c,d]

[a]*Univ Lyon, Univ Gustave Eiffel, Univ Claude Bernard Lyon 1, LBMC UMR_T 9406, F-69622 Lyon, France;*

stephane.nicolle@univ-eiffel.fr (S. Nicolle) and david.mitton@univ-eiffel.fr (D. Mitton)

[b]*École Normale Supérieure de Lyon, CNRS UMR5672, Laboratoire de Physique, F-69342 Lyon, France;*

jfpalier@ens-lyon.fr (J.-F. Palierne)

[c] *Univ Lyon, Université Lyon 1, INSERM, LYOS UMR 1033, 69008, Lyon, France;*

helene.follet@inserm.fr (H. Follet)

[d]*Centre Expert des Métastases Osseuses (CEMOS), Departement de Rhumatologie, Hôpital Lyon Sud, Hospices Civils de Lyon, Lyon, France;*

cyrille.confavreux@chu-lyon.fr (C.B. Confavreux)

*Corresponding author: Laboratoire de Biomécanique et de Mécanique des Chocs (LBMC), Université Gustave Eiffel – Campus de Lyon, case 24, 25 Avenue François Mitterrand 69675 Bron cedex, France. Tel.: +33 (0)472 14 23 50; Fax: +33 (0)472 37 68 37; e-mail: stephane.nicolle@univ-eiffel.fr (S. Nicolle)

Abstract

As far as their mechanical properties are concerned, cancerous lesions can be confused with healthy surrounding tissues in elastography protocols if only the magnitude of moduli is considered. We show that the frequency dependence of the tissue's mechanical properties allows for discriminating the tumor from other tissues, obtaining a good contrast even when healthy and tumor tissues have shear moduli of comparable magnitude. We measured the shear modulus $G^*(\omega)$ of xenograft subcutaneous tumors developed in mice using breast human cancer cells, compared with that of fat, skin and muscle harvested from the same mice. As the absolute shear modulus $\left|G^*(\omega)\right|$ of tumors increases by 42% (from 5.2 to 7.4 kPa) between 0.25 and 63 Hz, it varies over the same frequency range by 77% (from 0.53 to 0.94 kPa) for the fat, by 103% (from 3.4 to 6.9 kPa) for the skin and by 120% (from 4.4 to 9.7 kPa) for the muscle. These measurements fit well to the fractional model $G^*(\omega) = K(i\omega)^n$, yielding a coefficient *K* and a power-law exponent *n* for each sample. Tumor, skin and muscle have comparable *K* parameter values, that of fat being significantly lower; the *p*-values given by a Mann-Whitney test are above 0.14 when comparing tumor, skin and muscle between themselves, but below 0.001 when comparing fat with tumor, skin or muscle. With regards the *n* parameter, tumor and fat are comparable, with *p*-values above 0.43, whereas tumor differs from both skin and muscle, with *p*-values below 0.001. Tumor tissues thus significantly differs from fat, skin and muscle on account of either the *K* or the *n* parameter, *i.e.* of either the magnitude or the frequency-dependence of the shear modulus.

Keywords: shear viscoelastic properties, tumorous tissues, soft tissues, MR elastography

1. Introduction

Emerging imaging and computational tools in medicine require a solid knowledge of the mechanical properties of pathological and healthy tissues, key ingredients of the computational models used in clinical imaging and computer-assisted surgical techniques.

As a first example, finite element models are increasingly used for surgeons' training, for predicting the organ deformation during a needle biopsy or for developing non-rigid registration algorithms transforming images of an organ, taken at the time of diagnosis, to images projected during a conventional operation, robot-guided operation, or during radiotherapy (Tanner *et al.*, 2002; Samani *et al.*, 2004; Griesenauer *et al.*, 2017). Approximating the tissues in these models by simple linear elastic materials is often a first approach. However, the ability of FE models to correctly deform, provide the right haptic feel, or realistically distort preoperative images into intraoperative ones critically depends on the accuracy of mechanical models of tissues going beyond linear elasticity (Samani *et al.*, 2007; Pathmanathan *et al.*, 2008).

As a second example, the tissue elasticity measured using ultrasound or magnetic resonance elastography holds promise as a biomarker for cancer diagnostic in deep organs, the tumor usually being stiffer than the surrounding tissues (Hoyt *et al.*, 2008a; Glaser *et al.*, 2012; Ramião *et al.*, 2016; Samani *et al.*, 2007; Wells et Liang, 2011). First thought of as the virtual counterpart of the time-honored manual palpation, elastography initially used the linear elasticity theory to reconstruct the elasticity images of soft tissues from information on propagating sound waves (Krouskop *et al.*, 1998; Sarvazyan *et al.*, 2011; Wells et Liang, 2011; Gennisson *et al.*, 2013). Taking advantage of both the direct elastogram interpretation and the simpler algorithmic methods allowed by the linear elastic approach, a number of experimental works assess the Young modulus or the shear modulus (two linear elastic parameters) of soft tissues from *ex vivo* and *in vivo* protocols (Krouskop *et al.*, 1998; Lawrence *et al.*, 1998; McKnight *et al.*, 2002 ; Gennisson *et al.*, 2013).

In many situations, soft tissues are thus reduced to their isotropic linear elastic properties for computational reasons when they exhibit anisotropy and nonlinear viscoelasticity. However,

these last characteristics cannot always be ignored and can even be used in particular to improve the imaging tools and the interpretation of the resulting data to identify tumors.

For instance, in a preliminary work, Sinkus *et al.* (2000) surmised that tissue anisotropy could be used to distinguish benign from malignant tumors, the first ones being isotropic and the second ones anisotropic. However, Sinkus *et al.*, (2005) found later that some regions of healthy breast tissue can also be strongly anisotropic, making the tumor indistinguishable.

The large strain properties of tissues have been extensively studied as a most crucial feature to discriminate soft tissues. Generally, soft tissues stiffen as the deformation increases. Misinterpretation of results at different compression levels can thus occur when two neighboring tissues exhibit different nonlinear behaviors. In this regard, some studies provide contradictory results and opposite recommendations for the elastographic protocol: Krouskop *et al.* (1998) and Wellman *et al.* (1999) observed from compression tests on cancerous breast samples excised from patients that tumors exhibit stronger strain-nonlinearity than surrounding tissues, to the point that the tumors can be distinguished from healthy tissues at high compressive strain while they are indistinguishable from normal tissues at low compressive strain. The recommendation is then to increase the strain level during elastography to better discriminate the malignant tissues from the surrounding tissues. On the other hand, Barr and Zhang (2012), using elastography on patient's breast tissues in clinical situation, found that the contrast between Young's modulus of tumorous and normal tissues decreases with increasing strain, normal tissue stiffening more than cancerous tissue. Umemoto *et al.* (2014) reach the same conclusion through indentation tests on surgical samples of breast with cancerous lesions. These last two works then recommend that the practitioner minimizes the precompression to better distinguish tumorous tissues from the surrounding ones.

Viscoelastic properties of the tissues can also help discriminate benign from malignant tumors according to Sinkus *et al.* (2007) and Siegmann *et al.* (2010), the malignant ones having a more fluid behavior characterized by a higher loss (viscous) modulus than the benign ones. This

conclusion is however moderated by Xydeas *et al.* (2005), who stated that shear viscosity alone does not represent a good parameter for lesion classification.

Another feature of biological soft tissues seen as viscoelastic materials is that their modulus depends on the measurement frequency. First, together with the aforementioned large strain behavior, this could contribute to the disparity of reported 'elastic' moduli in the literature using elasticity instead of viscoelasticity when experiments are carried out at different frequencies. Second, the linear viscoelastic modulus of soft biological tissues generally increases with frequency, the increase rate depending on the tissue (Kiss *et al.*, 2004; Nicolle *et al.*, 2013; Yeung *et al.*, 2019). In this work, we use this frequency dependence to distinguish breast tumors from normal tissues. To this purpose, we compared the frequency-dependent behavior of tumor tissue based on human breast cancer cells developed subcutaneously in a murine model (Peyruchaud *et al*., 2001; Schmidt *et al.*, 2016) together with surrounding normal tissues such as fat, skin and muscle taken from the same mice. In order to avoid the abovementioned nonlinear stiffening, the viscoelastic behavior of each tissue is probed at very small strain.

2. Materials and Methods

2.1 Sample Origin

Using a xenograft model (Schmidt *et al.*, 2016), tumors were resected from immunocompromised six-week-old BALB/c nude female mice (Janvier Laboratories®) following a protocol approved by the Claude Bernard Lyon I University Ethical Committee for Animal Experimentation (DR2015-39).

Seven mice were anesthetized using an induction box with a 1 L air/min stream, 3% isoflurane concentration, and maintained with a mask at 2% isoflurane. The mice were then subcutaneously injected with MDA-B02 human breast cancer cells (Peyruchaud *et al*., 2001) - *B02 being cells isolated from human mammary carcinoma* - (2.10^6 cells in 100 µL Phosphate Buffered Saline (PBS) solution using a 1 mL syringe, Myjector 070151, Terumo Japan). After injection, tumor development was monitored through palpation and caliper, and as soon as its diameter was close

to 1 cm (more suitable for the subsequent mechanical test) or the surrounding tissues showed the first signs of necrosis, the tumor was resected after having anesthetized and euthanatized the mouse via cervical dislocation. The resected tumor was then immersed in phosphate-buffered saline (PBS) until preparation for the mechanical test performed on the same day.

For further comparison of mechanical properties with healthy tissues, skin, muscle and fat tissues were removed from each mouse in addition to the tumor. Skin was harvested from the abdomen and the legs, muscle was removed from legs and fat was removed from the abdomen.

2.2 Sample Preparation

Due to two tumors in an advanced state of necrosis, only five tumors (B02) out of seven planned were usable. Slices of an average thickness of 790 ± 2 µm (two slices by tumor) were cut by using a custom double-bladed scalpel as described in Nicolle *et al.* (2013). As tumors became necrotic before reaching a size large enough to cover the 10 mm diameter plates of the rheometer (Fig. 1), we adapted the measurement method to accommodate smaller and irregularly-shaped samples, as described in a forthcoming section.

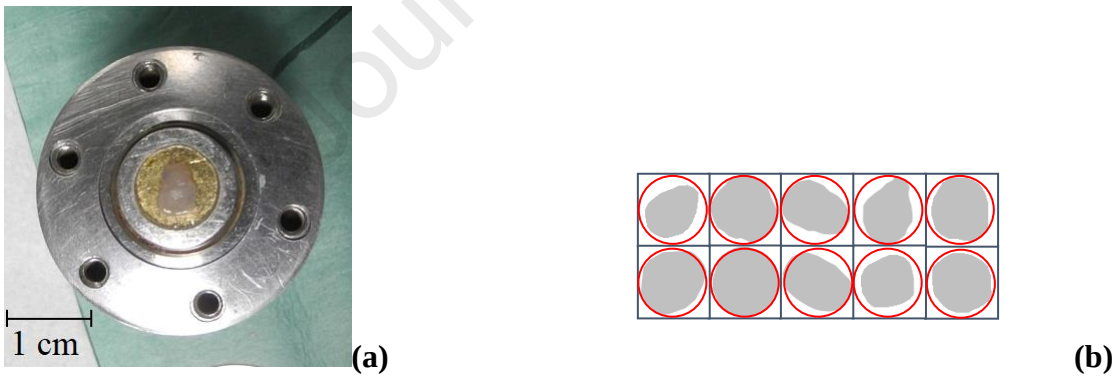

Figure 1: Typical sample too small to match the glass plate of the rheometer (a). Size of tumor B02 samples relative to the size of the glass plate (b).

The muscle samples were taken from the thighs with no particular attention paid to the direction of the fibers, although we are aware of the proven anisotropy of the muscle (Green *et al.*, 2013). The muscle slices were cut longitudinally along the femur, thus the fibers' direction lies

presumably in the slice plane. These samples covered the 10 mm diameter plates of the rheometer and were slightly compressed between the rheometer plates to make them flat. The final average thickness of muscle samples was 980 ± 160 µm.

Each piece of skin was first stripped from the underlying connective and adipose layers, and then cut using a punch to obtain a dermis sample of 10 mm diameter and of average thickness 590 ± 195 µm.

The fat samples were 'fluid' enough to fill the 10 mm diameter plates of the rheometer with about 500 µm thickness.

Once prepared, each sample was immediately immersed in a saline solution and preserved at 4°C until the test. The number of samples tested for each type of tissue is given in Table 1.

2.3 Mechanical Tests

The mechanical device used in this study is a custom squeezing deformation rheometer designed to determine the linear viscoelastic behavior of materials at acoustic frequencies. Samples are placed between parallel circular plates of r = 5 mm radius separated by an adjustable gap h. In order to prevent slip, the samples were glued to the plates using cyanoacrylate adhesive (Nicolle and Palierne, 2012). They were then surrounded with a saline solution in order to prevent dehydration of the tissue, according to Nicolle and Palierne (2010). The entire device was finally brought to body temperature (37°C) in a hermetic enclosure to prevent thermal gradients and water losses.

The upper plate of the rheometer is vertically driven by a piezoelectric actuator through an oscillatory motion $\delta^* = \delta_0 \, \mathrm{e}^{\mathrm{i}\omega t}$, of amplitude $\delta_0 = 2$ nm and angular frequency $\omega = 2\pi f$ [our use of complex quantities follows standard practice, see Appendix]. An incompressible sample with no-slip boundary condition then undergoes a squeezing deformation with a local Poiseuille parabolic displacement profile (Fig. 2). The typical shear applied to the sample is given by the following order of magnitude considerations. The volume displaced by the motion of the plate is

$\delta_0 r^2$ causing an outwards bulge of amplitude d and volume hrd at the edge (Fig. 2) where r and r^2 are the order of magnitude of the plate perimeter and area, respectively. Equating these volumes gives $d \sim \delta_0 r/h$, therefore the strain magnitude is of the order of $d/h \sim \delta_0 r/h^2$. With typical gap $h = 800$ μm, the strain order of magnitude is $d/h \sim \delta_0 r/h^2 \sim 2\times10^{-5}$, well within the linear regime, ensuring that the sample is not altered by the measurement.

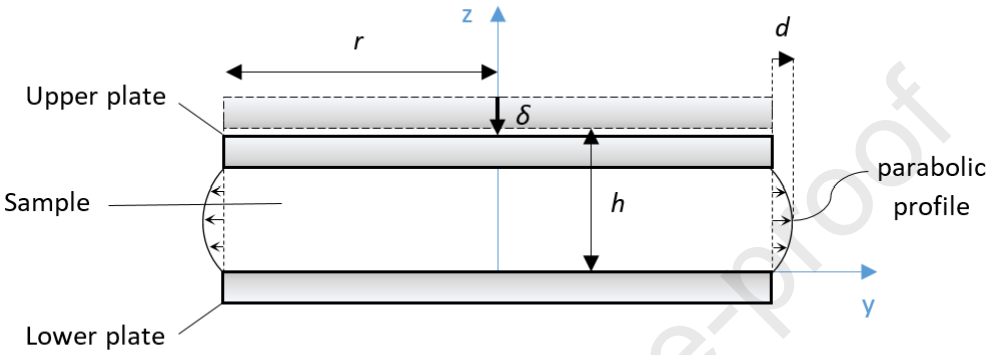

Figure 2: The upper plate of radius *r* is initially separated from the lower plate by a height *h*, then it is subjected to a vertical displacement δ which produces a parabolic-shaped bulge on the free edge of the sample whose the maximum displacement is *d*.

The lower plate registers the oscillatory transmitted force

$$F^* = (F' + \mathrm{i}F'')\mathrm{e}^{\mathrm{i}\omega t} \tag{1}$$

where F' and F'' are the in-phase and quadrature component of the complex force F^*, respectively. As derived in the Appendix, this force can be written as the product

$$F^* = \beta G^* \delta^* \tag{2}$$

being separately proportional to upper plate motion δ^*, to a shape factor β depending on the sample geometry, and to the sample's frequency-dependent complex shear modulus $G^*(\omega) = G'(\omega) + \mathrm{i}G''(\omega)$. The real and imaginary parts G' and G'' are real numbers named the storage and the loss modulus, respectively. The fact that G^* is complex is responsible for a phase

lag between the oscillating quantities F^* and δ^*, which is a characteristic of viscoelasticity. For circular plates of radius *r* separated by gap $h \ll r$, the shape factor assumes the analytic form $\beta = 3\pi r^4/2h^3$ (Reynolds 1886, our equation (A.11) with $A = B = r$). The tumor samples were too small to fill the rheometer plates; their shapes were thus recorded and the shape factor β was numerically computed for each of them according to equations (A.9)-(A.10) of Appendix, the Poisson equation (A.9) being numerically solved using Mathematica™ (Wolfram Research, Inc., 100 Trade Center Drive, Champaign, IL 61820-7237, USA, version 13.0). Precise shape determination however proved not to be critical since applying formula (A.11) to the best-fitting ellipse (having the same area and second order moments ratio as the sample shape), as given by ImageJ (National Institute of Health, Bethesda, USA, Rasband 1997-2012), produces β values within 4% of those exactly computed.

In short, the material viscoelastic modulus $G^* = F^*/\beta\delta^*$ is obtained from imposing the oscillatory displacement δ^*, determining the form factor β and measuring the transmitted force F^*.

We fit our measurements of $G^*(\omega)$ to the linear part of the model proposed in Kiss *et al.* (2004) and Nicolle *et al.* (2013) for biological soft tissues, drawing from Bagley and Torvik (1986). The frequency-dependent complex modulus $G^*(\omega)$ is written

$$G^* = K(\mathrm{i}\,\omega)^n = G' + \mathrm{i}G'', \quad \text{with} \quad G' = K\omega^n \cos\tfrac{n\pi}{2} \quad \text{and} \quad G'' = K\omega^n \sin\tfrac{n\pi}{2} \tag{3}$$

in terms of two parameters: the coefficient K (Pa·s^n) and the power-law exponent n (dimensionless). The absolute modulus is the positive real quantity

$$\left|G^*\right| = \sqrt{G'^2 + G''^2} = K\omega^n \tag{4}$$

The dimensionless parameter *n* characterizes the elastic/viscous balance, with $n = 0$ for elastic materials and $n = 1$ for Newtonian fluids. Graphically, *n* is the slope of $\left|G^*\right|$ *vs* ω in a log-log plot showing as a straight line, and *K* is the intercept at $\omega = 1$ rad s^{-1}, *i.e.* $f = 1/2\pi$ Hz.

A condition of physical admissibility is that *n* satisfies $0 \le n \le 1$ in order to prevent divergence of the relaxation modulus (Tschoegel 1989, Chap. 6). A characteristic of the power-law frequency dependence is that the loss ratio

$$\frac{G''}{G'} = \tan\frac{n\pi}{2} \tag{5}$$

is a function of *n* only, independent of frequency. This constant ratio is a strong property of power-law models, it follows from either $G' \propto \omega^n$ or $G'' \propto \omega^n$, as a consequence of causality (Tschoegl 1989, Chap. 8).

The material parameters (K, n) are obtained for each sample by fitting the power-law model (3) to the measured $G'(\omega)$ and $G"(\omega)$. We used the Levenberg-Marquardt algorithm provided by OriginPro2020™ (OriginLab Corporation, One Roundhouse Plaza, Suite 303, Northampton, MA 01060, United States, version 2020) to fit simultaneously G' and $G"$ with the same (*K*, *n*) parameters in "multi-data fit mode" by using "statistical" weighting, inversely proportional to the data value, thus minimizing the quantity

$$\chi^2 = \sum_i \frac{\left(G_i' - K\omega_i^n \cos\frac{n\pi}{2}\right)^2}{G_i'} + \frac{\left(G_i'' - K\omega_i^n \sin\frac{n\pi}{2}\right)^2}{G_i''} \tag{6}$$

where the sum extends to the 13 measurement frequencies $\omega_i = 2\pi f_i$, $f_i = 10^{(i-4)/5}$ Hz $= 0.251 \cdots 63.1$ Hz, $i = 1 \cdots 13$, spanning 2½ decades. Such weighting increases the fit sensitivity to $G"$, of comparatively smaller magnitude than G'.

We performed two-by-two statistical comparisons of the *n* and *K* parameters distributions of the different tissues using a nonparametric Mann-Whitney test (provided by OriginPro2020™, with a 0.05 significance level). The inter-sample variability of experimental data was also examined in relation to the variability of the model parameters.

3. Results

The power-law model (3) is fit to the measured $G'(\omega)$ and $G''(\omega)$ for each one of the 39 samples. For the four different tissues under investigation, namely B02 tumor, muscle, skin and fat, the distribution of the fitted *K* and *n* parameters is given in Figure 3 and 4, and the average *K* and *n* are reported in Table 1. The standard deviations given therein are inter-sample variabilities, whereas the fitting uncertainty for the *K* and *n* value associated with each given sample is much lower, about one tenth of the inter-sample variability. The relative inter-sample variability of *K* is 80% for fat and 50-55% for the other tissues; these values are typical of material constants of biological tissues (Cook *et al.*, 2014). The relative inter-sample variability of the index *n* is comparatively smaller, being about 7% to 24%. [Strictly speaking, since the physical dimension of *K* is $\mathrm{Pa}\cdot\mathrm{s}^n$, in comparing different *K* we compare values of $K/\left(1\mathrm{Pa}\cdot\mathrm{s}^n\right)$, *i.e.* the numerical value of *K* in the MKS unit system.]. In addition, it can also be noted from Figure 5 that the intra-individual variability ($K = 3600 \pm 2600$; $n = 0.13 \pm 0.01$) represents a major contribution to the total population variability ($K = 3160 \pm 1710$; $n = 0.133 \pm 0.009$ in Table 1) for skin.

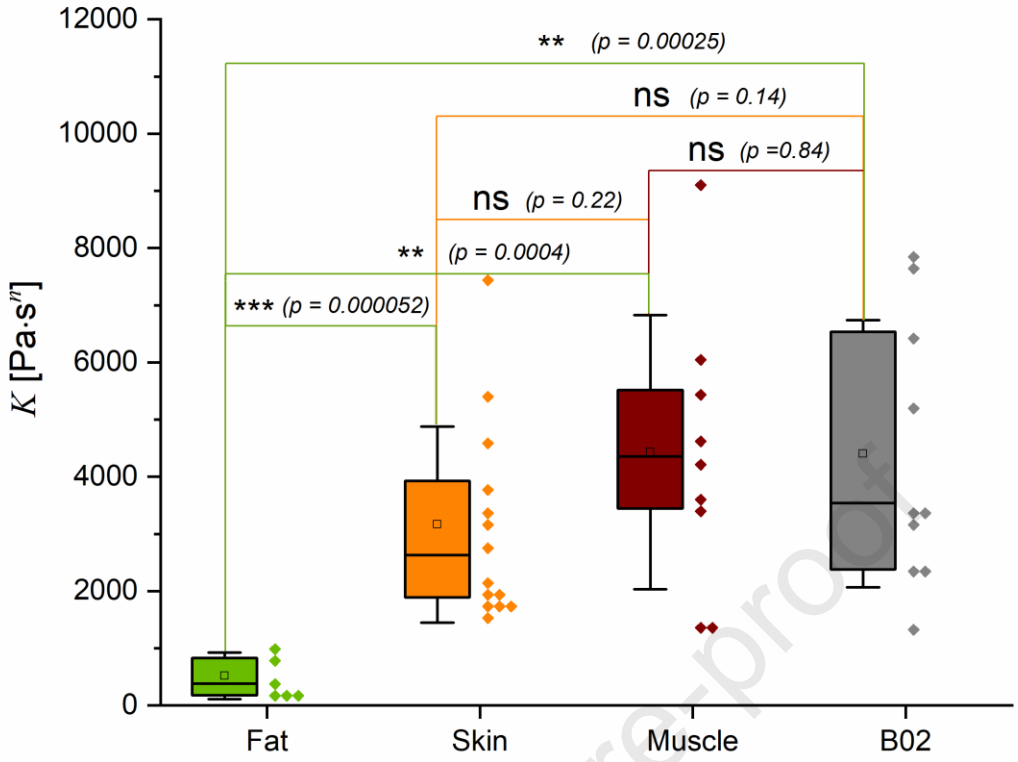

Figure 3: Distribution of the parameter *K* (dynamic modulus at ω = 1 rad/s, coming from the fit of all results obtained for each tissue. The set of data (diamonds) is represented for each distribution. Comparison of these distributions by using a nonparametric Mann-Whitney test: (ns) non-significant, (*) significant (*p*-value < 0.05), (**) very significant (*p*-value < 0.001), (***) extremely significant (*p*-value < 0.0001). B02: subcutaneous tumor (human breast cancer cells (B02))

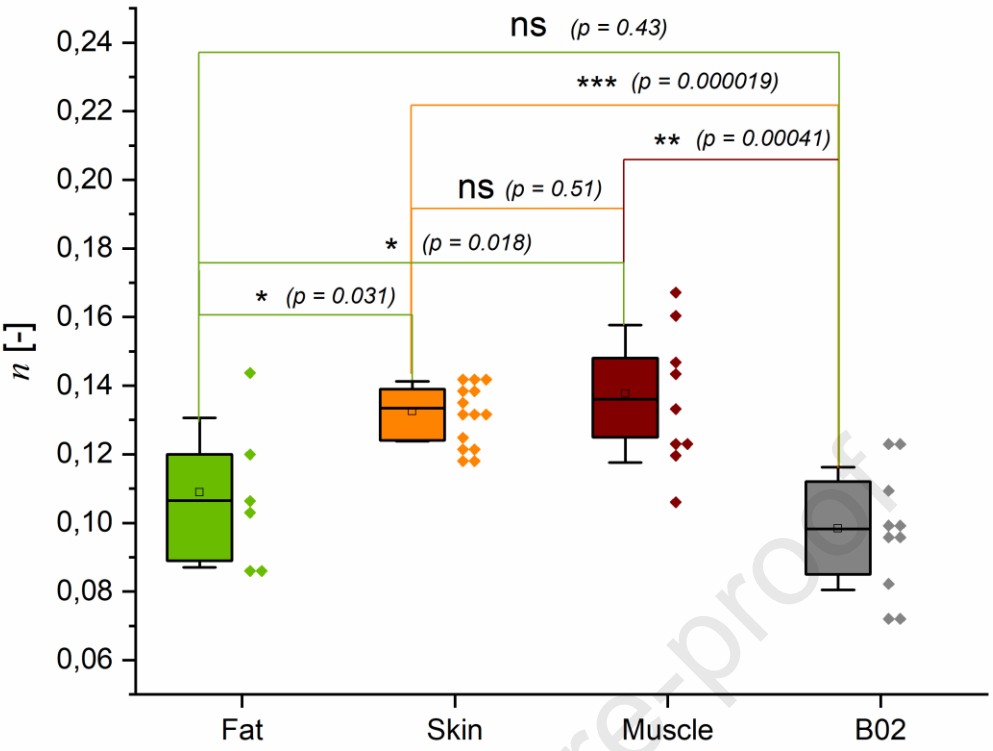

Figure 4: Distribution of the parameter *n* (frequency-dependence of the dynamic modulus), for all tissue samples. Comparison of these distributions by using a nonparametric Mann-Whitney test: (ns) nonsignificant, (*) significant (p-value < 0.05), (**) very significant (p-value < 0.001), (***) extremely significant (p-value < 0.0001). B02: subcutaneous tumor (human breast cancer cells (B02))

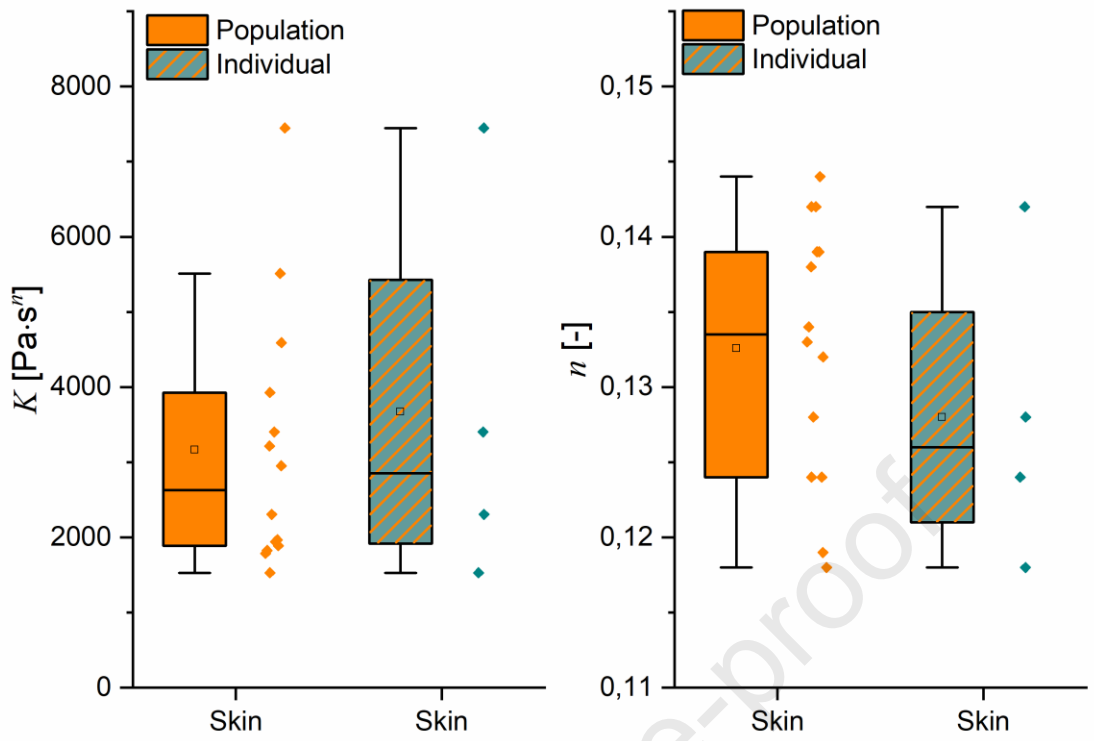

Figure 5: Distribution of the model parameters *K* and *n* for the entire population of skin samples (14 samples), and for skin samples from a single individual (4 samples).

	#	K (Pa·s^n)	n (-)
B02	10	4400 ± 2340	0.098 ± 0.018
Muscle	9	4430 ± 2400	0.138 ± 0.020
Skin	14	3160 ± 1710	0.133 ± 0.009
Fat	6	520 ± 400	0.109 ± 0.022

Table 1: Average material parameters of the fractional model (3) for mice tissues: subcutaneous inter-sample variabilities, which are about ten times the parameters fitting precision for each given sample.

The average moduli G' and G'' of tumor, muscle, skin and fat tissue are plotted versus frequency on Figure 6, together with the model response according to equation (3) using the average material parameters given in Table 1; the coefficient of determination R^2 averages to 0.95

for G' and 0.68 for G'' [in calculating R^2, G' and G'' values are separately referred to their respective average. Referring them to their common average would result in an unnaturally high R^2, about 0.99]. For any given sample, the measured G' and G'' and their fit by equation (3) look very similar to the averages reported in Figure 6. Although not warranted in general for non-linear models (Robertson and Cook, 2014), the fact that our model (3), provided average K and n parameters, gives such a good fit to the average G' and G'' is due to the fact that it is linear in K and that the only non-linear parameter, n, has a quite low variability, less than 2.2% of its (0...1) admissible range, thus making the fit an almost linear fit over K only.

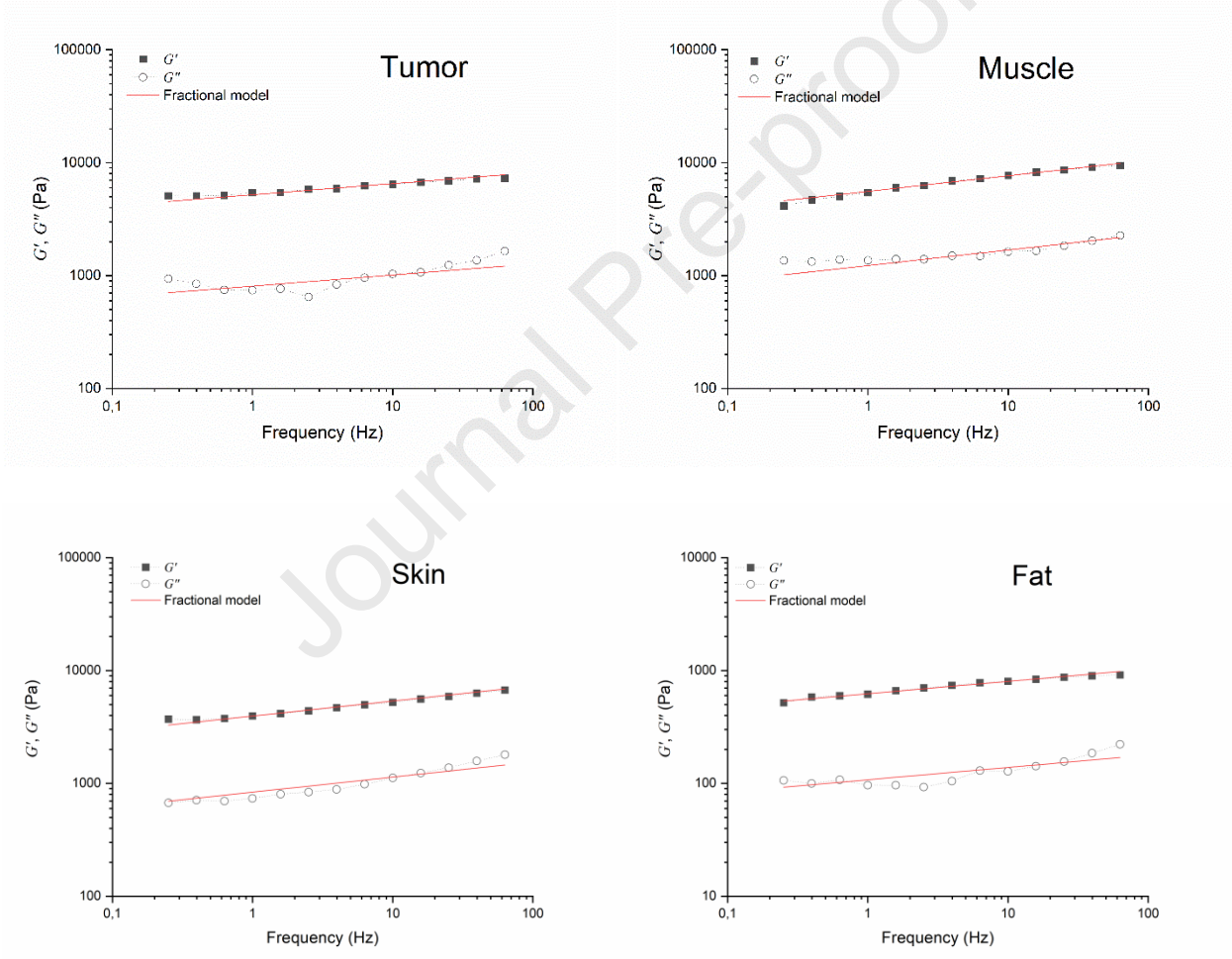

Figure 6: Symbols: average storage and loss modulus *vs* frequency of B02 tumor muscle, skin and fat. Continuous lines: fit by model (3) using the parameters of Table 1. B02 tumor: $R^2 = 0.864$ for G' and 0.617 for G'', Muscle: $R^2 = 0.982$ for G' and 0.602 for G'', Skin: $R^2 = 0.971$ for G' and 0. 873 for G'', Fat: $R^2 = 0.979$ for G' and 0.636 for G''.

Figure 3 and Table 1 show that the parameter *K* is quite similarly distributed for B02 tumor, muscle and skin tissues, the only tissue with a recognizably different distribution of *K* being fat. A Mann-Whitney test finds significant differences only between fat and the other tested tissues, as reported on Figure 3. By contrast, as shown in Figure 4 and Table 1, the distributions of parameter *n* reveal two different groups: the low-*n* fat and B02 tumor tissues, with *n* about 0.10, and the (relatively) high-*n* muscle and skin, with *n* about 0.13. The Mann-Whitney test reveals no significant difference between (high-*n*) muscle and skin, on the one hand, and between (low-*n*) fat and B02 tumor, on the other hand, whereas significant differences appear between low-*n* and high-*n* tissues (Figure 4).

The aim of this study, differentiating B02 tumorous tissue from healthy tissues, cannot be realized by just comparing the measured moduli. Figure 7a displays the average storage and loss moduli of all tested tissues: it appears clearly that, within the entire explored frequency range, tumor, skin and muscle are bunched together and can only be set apart from fat. Indeed, the inter-sample variability of G' and G'' is dominated by the variability of the *K* parameter, of 50% to 80% relative value, comparable with the spread of the average G' or G'' for tumor, skin and muscle. The same issue arises when considering the absolute modulus $|G^*|$, which is the only quantity reported in some studies: Figure 7b shows a similar confusion of $|G^*|$ for tumor, skin and muscle, the only tissue standing out being fat.

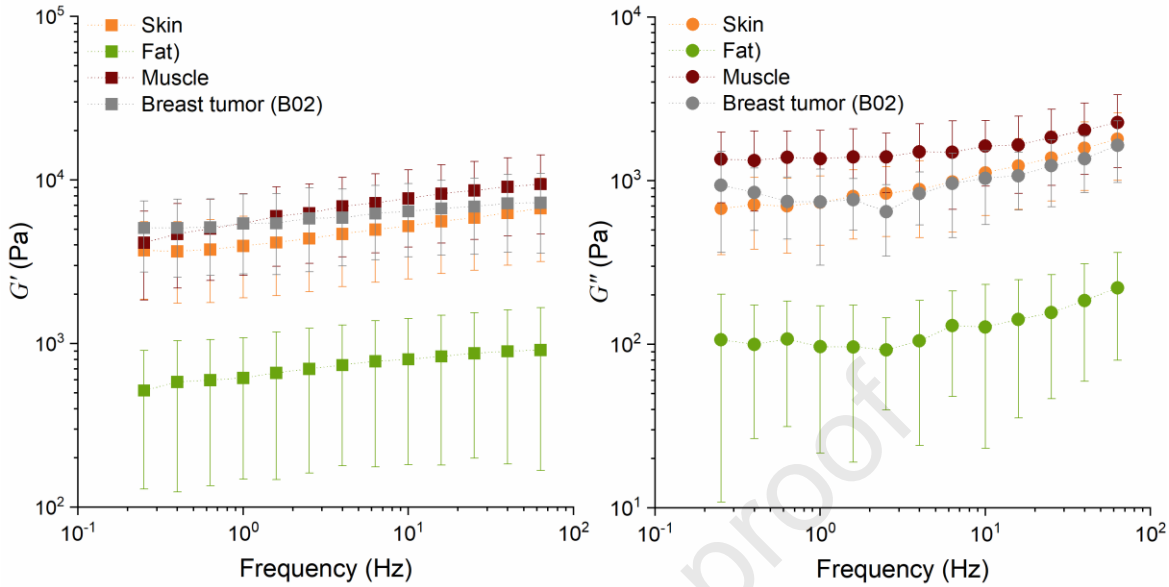

(a)

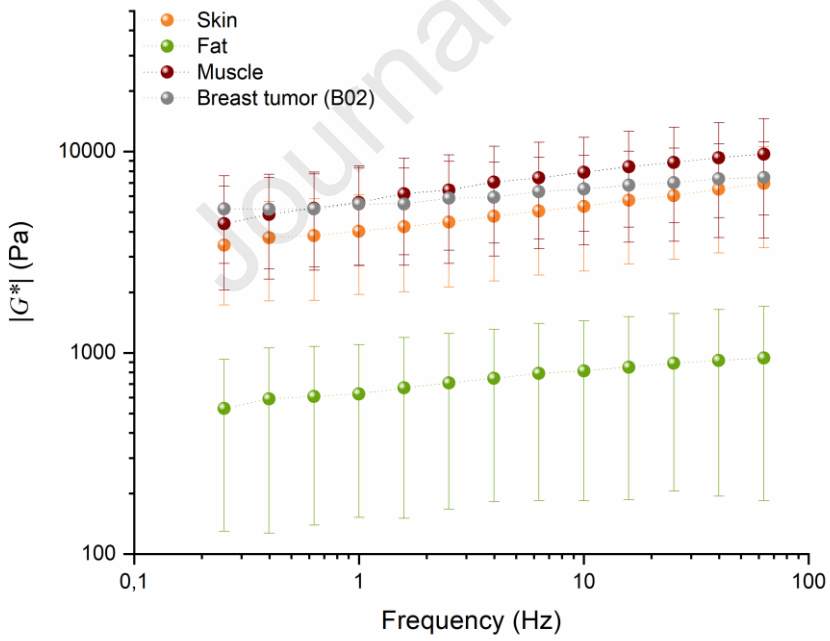

(b)

Figure 7: Average experimental values and respective standard deviation of (a): storage (G') and loss (G'') moduli, (b): absolute shear modulus ($|G^*|$)

Examining the model parameters K and n however brings a clearer perspective: the fat being singled out due to its very low K, the tumor's lower n (0.10) can be distinguished from skin and muscle's higher n (0.13). Tumor B02 (n = 0.098) thus appears as the most elastic tissue compared to fat (n = 0.104), skin (n = 0.133) and muscle (n = 0.134), its lower n value making its modulus less frequency-dependent. Over the 0.25–63 Hz frequency range we explored, the modulus of the tumor increases by 42%, from 5.2 kPa to 7.4 kPa, whereas that of fat increases by 77%, from 0.53 kPa to 0.94 kPa, that of skin increases by 103%, from 3.4 kPa to 6.9 kPa, and that of muscle increases by 120%, from 4.4 kPa to 9.7 kPa.

4. Discussion

New clinical tools such as elastography and computational patient-specific models require a solid knowledge of the mechanical properties of pathological and healthy soft tissues, a task made difficult by the anisotropy, the nonlinearity and the viscoelasticity of soft tissues. This explains in part the disparity of the properties reported in the literature under various experimental protocols.

Because soft tissues are viscoelastic, we propose that healthy and pathological tissues be distinguished not only according to their moduli but also by considering the frequency dependence of these moduli. Tissue's viscoelasticity is related to their microstructure, roughly speaking to the density and arrangement of cells, as well as the network of fibers such as collagen. Cross-links in the fiber network contribute to elasticity, while loose and dangling parts of the network add to the viscosity (Sack *et al.*, 2013). In particular, due to excessive and uncontrolled remodeling of the extracellular fiber matrix, tumor tissues are known to be stiffer and more elastic (i.e. less frequency-dependent) than normal tissues (Cox and Erler, 2011; Pepin *et al.*, 2015; Li *et al.*, 2019).

In this study, we observe that the shear modulus of the tumor tissue clearly differs from that of the fat, by almost an order of magnitude. It is however very close to that of the skin and muscle, making the tumor indistinguishable from such fibrous tissues. However, the modulus' frequency dependence, characterized by the fractional exponent n, is lower for the tumor (n =

0.098) than for the skin (n = 0.133) and the muscle (n = 0.138), although statistically indistinguishable from that of fat (n = 0.109). This means that the tumors appear more elastic than surrounding tissues in accordance with the abovementioned remodeling of their extracellular matrix.

The primary importance of the moduli's frequency dependence warrants reliable experimental determinations. The model (3) predicts that log-log plots of G' and G'' versus ω are straight lines, the gap between them, ruled by (5), being univocally related to their common slope n. Mechanical measurements perform properly in this respect (our results, Kiss *et al*. (2004), Holt *et al.* (2008)). By contrast, MRE (magnetic resonance elastography) seems inclined to produce moduli $G' \propto \omega^n$ and $G'' \propto \omega^n$, according to (3), with however an exponent n greater than the value $2/\pi \arctan G''/G'$ prescribed by relation (5) (Sack *et al.*, 2009, Riek *et al.*, 2011); even greater than 1, the limit of physically possible exponents (Sinkus *et al.*, 2007, Bohte *et al.*, 2017). Papazoglou *et al.* (2012) present both mechanical and MRE data on agar-based gels mimicking biological tissues: whereas their mechanical data agree with our equations (3) and (5), their MRE data show the aforementioned tendency to higher exponents n. MRE is thus a promising technique, as it allows *in vivo* mechanical measurements, but not yet wholly reliable in the assessment of frequency dependence.

That the tumor is more elastic than the healthy tissues is corroborated by Sack *et al.* (2013) who observed that the exponent n slightly decreases with the fibrosis grade of liver, decreasing from 0.266 for a normal liver to 0.238 for a fibrotic liver of grade F4, in relation with the densification of the extracellular matrix occurring in tumorous tissue. This conclusion is confirmed by Sauer *et al.* (2019) who proved that the power law exponent decreases with an additional crosslinking of the collagen network composing the stromal tissue.

The mechanical properties found in this study are compared with those reported in the literature in Table 2. Despite differences in origin of the samples, in techniques and protocols used, the current data are found to be consistent with the values presented in this Table, which reports both *in vitro* and *in vivo* studies. The comparison *in vivo*/*in vitro* is never straightforward in the

mechanical studies since the deformation geometry is controlled *in vitro* but the physiological conditions are not strictly satisfied, causing postmortem effects (Chatelin *et al.*, 2011), while the *in vivo* conditions preclude an exact control of the deformation geometry. Nevertheless, our rheometric data converge in magnitude with those coming from MRE, which shows that the *in vitro* conditions applied in the current study (saline solution at body temperature for hydrating the tissue during the test, according to Nicolle and Palierne (2010)) satisfactorily reproduce the *in vivo* conditions of MRE. This is supported by Kerdok *et al.* (2006), who found similar moduli in mechanical measurements on *in vivo* and *ex vivo* liver, perfused with a saline solution at body temperature. Contrary to their protocol, however, our tissue samples are hydrated but not pressurized. How pressurization affects the tissue viscoelasticity remains to be determined; moreover, as discussed by Kerdok *et al*, these effects are likely organ-dependent.

At this stage, it can be stated that when the tumor tissues and the surrounding tissues have comparable stiffness, a multi-frequency assessment of the small-strain shear modulus is in order, to facilitate the distinction of a tumor from a healthy tissue environment, in particular in the cases of benign tumors and suspicious lesions sought using MRE protocols.

A concern of this study is whether the tested tumors are representative of breast cancers. Although human in origin, the tumor cells were developed subcutaneously in mice instead of human breasts. The comparison of the viscoelastic properties was made between the tumor, the skin and the muscle coming from different anatomical regions in mice, not with the surrounding tissues present in the breast, such as the adipose and the fibroglandular tissues. It would be worthwhile to validate the present observations and conclusions on pathological breast tissues resected from patients.

5. Conclusions

The methods developed in this study allow measuring irregularly shaped samples of centimeter size to assess their viscoelastic properties in *in vitro* conditions. By comparing subcutaneous tumor with fat, muscle and skin in a murine model, we show that the frequency

dependence of the tissues' viscoelastic properties allows distinguishing tumors from other soft tissues, even of comparable moduli, the tumor's modulus being less frequency-dependent than that of normal tissues. The present results thus call for a deeper investigation of the viscoelastic properties of healthy (adipose and fibroglandular tissues) and pathological breast tissues at different grades (fibroadenoma and carcinoma tissues).

Skin	**Species**	**Exp. Techniques**	**$\|G^*\|$ at 1 Hz**	**Exponent *n***
Current Study	mouse	rheometer	4 kPa	0.133
Nicolle *et al.* (2017)	rat	rheometer	7.3 kPa	0.137
Lamers *et al.* (2013)	human	rheometer	2.7 kPa	-
Rieger and Deem (1974)	human	tensile tests	-	0.173
Holt *et al.* (2008)	human	rheometer	-	0.16
Corr *et al.* (2009)	porcine	tensile tests	-	0.17 – 0.22

Muscle	**Species**	**Exp. Techniques**	**$\|G^*\|$ at 1 Hz**	**Exponent *n***	**$\|G^*\|$ at 140 Hz**	**$\|G^*\|$ between 200 Hz and 800 Hz**
Current Study	mouse	rheometer	5.6 kPa	0.138	11.3 kPa†	11.9 to 14.5 kPa† ;$\|G^*\| = 4430\omega^{0.138}$
Tan et al. (2015)	bovine	rheometer	5.7 kPa	-	-	-
Hoyt *et al.* (2008b)	human	sonoelastography	-	-	9.95 kPa	-
Riek *et al.* (2011)	bovine	MR elastography	-	0.25	-	12.25 to 35.9 kPa†;$\|G^*\| = 3640\omega^{0.25}$

Fat	**Species**	**Exp. Techniques**	**$\|G^*\|$ at 0.1 Hz**	**$\|G^*\|$ at 40 Hz**	**$\|G^*\|$ at 63 Hz**
Current Study	mouse	rheometer	0.49 kPa†	0.92 kPa	0.94 kPa
Samani *et al.* (2007)	human	indentation tests	1.1 kPa‡	-	-
Chen *et al.* (2013)	human	MR elastography	-	0.33 kPa	-
Lawrence *et al.* (1998)	human	MR elastography	-	-	0.43 kPa between 50 and 100 Hz
Lorenzen *et al.* (2002)	human	MR elastography	-	-	0.5 to 4 kPa (median = 2 kPa)

† Using our Eq. (3) with material parameters from Table (1).
‡ Young's modulus / 3 (owing to incompressibility)

Table 2: Comparison of the current data to the literature ($|G^*|$ is the absolute shear modulus, the exponent *n* characterizes the frequency-dependence of the shear modulus through the power law $|G^*| = K\omega^n$)

Appendix: deformation of a sample of arbitrary shape in the rheometer

Reynolds (1886) considered the squeeze flow of a Newtonian fluid as a special case of lubricating flow; here we extend his equations (9-29) to linear viscoelasticity in harmonic regime and to arbitrary geometry. [We follow the IUPAC recommendations pertaining to linear viscoelasticity (Kaye *et al.* 2008, §5): Asterisks designate complex quantities, being either oscillating quantities, here $\delta^*, \mathbf{d}^*, p^*, \boldsymbol{\sigma}^*$ or F^*, whose real part corresponds to the physical quantity, or (non-oscillating) ratios of oscillating quantities such as G^*, assuming non-real values when there is a phase lag between these quantities.]

The sample is a slab of thickness h and arbitrary section S, placed between two plates, its upper and lower faces following the corresponding plate's motion without slip; the upper face thus moving by $\delta^* = \delta_0 \, \mathrm{e}^{\mathrm{i}\omega t}$ in the perpendicular direction whereas the lower face remains fixed. Let the upper and lower plates be in the (x-y)-plane at $z = h + \delta^*$ and $z = 0$, respectively. Assuming $\delta_0 \ll h$, calculations will be carried out at linear order in δ_0 / h, within the frame of linear viscoelasticity, and, in the lubrication approximation (Reynolds 1886), at the lowest significant order in $h/r \ll 1$ (r being a typical linear extension of surface S, its radius if S is circular).

The no-slip boundary conditions for the space- and time-dependent displacement field $\mathbf{d}^*(x, y, z, t)$ read

$$\begin{cases} \mathbf{d}^* = \mathbf{0}, & z = 0 \\ \mathbf{d}^* = d_z^* \mathbf{e}_z = \delta^* \mathbf{e}_z, & z = h \end{cases} \tag{A.1}$$

with $\mathbf{e}_z$ the unit vector in the z-direction. The material obeys the incompressibility condition

$$\nabla \cdot \mathbf{d}^* = 0 \tag{A.2}$$

where ∇ is the three-dimensional gradient operator, and the dynamics equation reduces to

$$\nabla p^* = G^* \Delta \mathbf{d}^* \tag{A.3}$$

where $\Delta = \nabla^2$ is the Laplacian operator, when the inertial term $\rho \partial^2 \mathbf{d}^* / \partial t^2 = -\rho\omega^2 \mathbf{d}^*$ is negligible, *i.e.* when $\left| \rho\omega^2 \mathbf{d}^* / G^* \Delta \mathbf{d}^* \right| \sim \omega^2 \tau^2 \ll 1$, where $\tau = h\sqrt{\rho / |G^*|}$ is the characteristic time of transverse waves [in our measurements, $|G^*| \sim 10^3\,\mathrm{Pa}$, $\rho \sim 10^3\,\mathrm{kg\,m^{-3}}$ and $h \sim 10^{-3}\,\mathrm{m}$, therefore $\tau \sim 10^{-3}\,\mathrm{s}$; this sets an upper frequency limit $f = \omega / 2\pi < 1/2\pi\tau = 160\,\mathrm{Hz}$].

The displacement is written as the sum of a Poiseuille parabolic profile $\mathbf{d}_\perp^*$ parallel to the plates, driven by the pressure gradient, and a *z*-component $d_z^* \mathbf{e}_z$ obeying boundary conditions (A.1):

$$\mathbf{d}^* = \mathbf{d}_\perp^* + d_z^* \mathbf{e}_z, \qquad \mathbf{d}_\perp^* = -\frac{z(h-z)}{2G^*} \nabla_\perp p^* \tag{A.4}$$

with $\nabla_\perp = \mathbf{e}_x \partial / \partial x + \mathbf{e}_y \partial / \partial y$. Rewriting the divergence of the displacement as $\nabla \cdot \mathbf{d}^* = \nabla_\perp \cdot \mathbf{d}_\perp^* + \partial d_z^* / \partial z$, integrating incompressibility condition (A.2) over z from 0 to h and using boundary conditions (A.1) results in

$$\Delta_\perp p^* = \frac{12}{h^3} G^* \delta^* \tag{A.5}$$

where $\Delta_\perp = \nabla_\perp^{\,2} = \partial^2 / \partial x^2 + \partial^2 / \partial y^2$ is the two-dimensional Laplacian. The boundary condition for the pressure is that it vanishes at the edge of the sample, i.e. on the boundary ∂S of S:

$$p^*(x, y) = 0 \quad \text{for } (x,y) \in \partial S \tag{A.6}$$

A fundamental feature of squeezing deformations is that the typical magnitude of $\mathbf{d}_\perp$ is much greater than that of d_z^*: Because the sample volume is constant, outward (resp. inward) bulging of the sample edge occurs when the plates get closer (resp. farther away). The perimeter length is $\sim r$, the area of the free surface at the sample edge is thus $\sim hr$ and the bulge volume is $\sim hr\, d_\perp^*$, equal to the volume $S\delta^*$ swept by the upper plate motion, so we have $d_\perp^* \sim \delta^* r / h$ with $r \gg h$. Since the *z*-component magnitude is $d_z^* \sim \delta^*$, one has

$$d_\perp^* \sim \frac{r}{h} d_z^* \gg d_z^* \sim \delta^* \tag{A.7}$$

The force on the plates obtains by integrating the surface force $\boldsymbol{\sigma}^* \cdot \mathbf{e}_z = G^*\left(\nabla \mathbf{d}^* + (\nabla \mathbf{d}^*)^T\right) \cdot \mathbf{e}_z - p^* \mathbf{e}_z$ over S at $z = h$. According to (A.5), the pressure magnitude is $p^* \sim G^* \delta^* S / h^3$, whereas due to condition (A.1) the only non-zero component of $G^*\left(\nabla \mathbf{d}^* + (\nabla \mathbf{d}^*)^T\right)$ at $z = h$ is $G^* \partial \mathbf{d}^* / \partial z = h \nabla_{\square} p^* / 2 + G^* \mathbf{e}_z \partial d_z / \partial z$, negligible with respect to p^* since $h \nabla_{\square} p^* \sim h p^* / r \sim G^* \delta^* r / h^2$ and $G^* \partial d_z / \partial z \sim G^* \delta^* / h$. The force the material exerts on the upper plate is then in the *z*-direction and reduces to

$$F^* = -\int_S p^* \mathrm{d}S \tag{A.8}$$

The solution to the problem then follows: Let the function $\phi(x, y) \geq 0$ be defined within S and on the boundary ∂S, such that

$$\begin{cases} \Delta\phi = -1 & \text{within } S \\ \phi = 0 & \text{on } \partial \mathrm{S} \end{cases} \tag{A.9}$$

then the pressure (A.5) reads $p^* = -\dfrac{12}{h^3} G^* \delta^* \phi$ and the force F^* can be written $F^* = \beta G^* \delta^*$, where

$$\beta = \frac{12}{h^3} \int_S \phi \, \mathrm{d}S \tag{A.10}$$

As an example, when S is an ellipse of semi-axes A and B along the *x*- and *y*-axes, one has $\phi = \left(1 - x^2/A^2 - y^2/B^2\right) \Big/ \left(2/A^2 + 2/B^2\right)$, therefore

$$\beta = \frac{3\pi}{h^3} \frac{A^3 B^3}{A^2 + B^2} \tag{A.11}$$

Acknowledgements

The authors are deeply grateful to Lamia Bouazza and Sandra Geraci for their technical supports on cells development and animals' experiment, and with the use of the ALECS platform. This work was partly funded by LabEx Primes (ANR-11-LABX-0063) and MSD AVENIR Research Grant (CBC), and Philippe Clézardin (Labex DevWeCan).

References

Bagley, R.L., Torvik, P.J., 1986. On the fractional calculus model of viscoelastic behavior. Journal of Rheology 30(1), 133-155. https//doi.org/10.1122/1.549887

Barr, R.G., Zhang, Z., 2012. Effects of precompression on elasticity imaging of the breast. Journal of Ultrasound in Medicine 31(6), 895-902. https//doi.org/10.7863/jum.2012.31.6.895

Bohte, A.E., Nelissen, J.L., Runge, J.H., Holub, O., Lambert, S.A., de Graaf, L., Kolkman, S., van der Meij, S., Stoker J., Strijkers, G.J., Nederveen, A.J., Sinkus, R., 2017. Breast magnetic resonance elastography: a review of clinical work and future perspectives. NMR in Biomedicine 31:e3932. https//doi.org/10.1002/nbm.3932

Chatelin, S., Oudry, J., Périchon, N., Sandrin, L. Allemann, P., Soler, L., Willinger, R., 2011. *In vivo* liver tissue mechanical properties by transient elastography : Comparison with dynamic mechanical analysis. Biorheology 48, 75-88. https//doi.org/10.3233/BIR-2011-0584

Chen J., Brandt K., Ghosh K., Grimm R., Glaser K., Kugel J., Ehman R., 2013. Noncompressive MR elastography of breasts. Proceedings of the International Society of Magnetic Resonance Medicine 21, 1736. https://archive.ismrm.org/2013/1736.html

Cook, D., Julias, M., Nauman, E., 2014. Biological variability in biomechanical engineering research: Significance and meta-analysis of current modeling practices. Journal of Biomechanics 47, 1241-1250. https//doi.org/10.1016/j.jbiomech.2014.01.040

Corr, D.T., Gallant-Behm, C.L., Shrive, N.G., Hart, D.A., 2009. Biomechanical behavior of scar tissue and uninjured skin in a porcine model. Wound Repair and regeneration 17, 250-259. https//doi.org/10.1111/j.1524-475X.2009.00463.x

Cox, T.R., Erler, J., T., 2011. Remodeling and homeostasis of the extracellular matrix: implications for fibrotic deseases and cancer. Disease Models and Mechanisms 4, 165-178. https//doi.org/10.1242/dmm.004077

Gennisson JL, Deffieux T, Fink M, Tanter M., 2013. Ultrasound elastography: principles and techniques. Diagnostic and Interventional Imaging 94(5), 487-495. https//doi.org/10.1016/j.diii.2013.01.022

Glaser, K.J., Manduca, A., Ehman, R.L., 2012. Review of MR elastography applications and recent developments. Journal of Magnetic Resonance Imaging 36(4), 757-774. https//doi.org/10.1002/jmri.23597

Green, M.A., Geng, G., Qin, E., Sinkus, R., Gandevia, S.C., Bilston, L.E., 2013. Measuring anisotropic muscle stiffness properties using elastography. NMR in Biomedicine 26, 1387-1394. https//doi.org/10.1002/nbm.2964

Griesenauer, R.H., Weis, J.A., Arlinghaus, L.R., Meszoely, I.M., Miga, M.I., 2017. Breast tissue stiffness estimation for surgical guidance using gravity-induced excitation. Physics in Medicine and Biology 62(12), 4756-4776. https//doi.org/10.1088/1361-6560/aa700a

Holt, B., Tripathi, A., Morgan, J., 2008. Viscoelastic response of human skin to low magnitude physiologically relevant shears. Journal of Biomechanics 41, 2689-2695. https//doi.org/10.1016/j.jbiomech.2008.06.008

Hoyt, K., Castaneda B., Zhang, M., Nigwekar P., Di Sant'Agnese, P.A., Joseph, J.V., Strang, J., Rubens, D.J., Parker, K.J., 2008a. Tissue elasticity properties as biomarkers for prostate cancer. Cancer Biomarkers 4(4-5), 213-225. https//doi.org/10.3233/CBM-2008-44-505

Hoyt, K., Kneezel, T., Castaneda, B., Parker, K.J., 2008b. Quantitative sonoelastography for the in vivo assessment of skeletal muscle viscoelasticity. Physics in Medicine & Biology 53(15), 4063-4080. https//doi.org/10.1088/0031-9155/53/15/004

Kaye, A. Stepto, R. F. T., Work, W. J.,. Alemán, J. V, Malkin, A. Ya., 2009. Definitions of terms relating to the non-ultimate mechanical properties of polymers (Recommendations 1998), Pure and Applied Chemistry 70(3), 701-754. https//doi.org/10.1351/pac199870030701

Kerdok, A.E., Ottensmeyer, M.P., Howe, R.D., 2006. Effects of perfusion on the viscoelastic characteristics of liver. Journal of Biomechanics 39, 2221-2231. https//doi:10.1016/j.jbiomech.2005.07.005

Kiss, M.Z., Varghese, T., Hall, T.J., 2004. Viscoelastic characterization of in vitro canine tissue. Physics in Medicine and Biology 49, 4207-4218. https//doi.org/10.1088/0031-9155/49/18/002

Krouskop, T.A., Wheeler, T.M., Kallel, F., Garra, B.S., Hall, T., 1998. Elastic moduli of breast and prostate tissues under compression. Ultrasonic Imaging 20(4), 260-274. https//doi.org/10.1177/016173469802000403

Lawrence, A.J., Muthupillai, R., Rossman, P.J., Smith, J.A., Manduca, A., Ehman, R.L., 1998. Magnetic resonance elastography of the breast: Preliminary experience. Proceedings of the International Society for Magnetic Resonance in Medicine, Sydney, Australia. Magnetic Resonance Elastography of the Breast - ISMRM http://cds.ismrm.org › ismrm-1998

Lamers, E., van Kempen, T.H.S., Baaijens, F.P.T., Peters, G.W.M., Oomens, C.W.J., 2013. Large amplitude oscillatory shear properties of human skin. Journal of the Mechanical Behavior of Biomedical Materials 28, 462-470. https//doi.org/10.1016/j.jmbbm.2013.01.024

Li, J., Zormpas-Petridis, K., Boult, J.K.R., Reeves, E.L., Heindl, A., Vinci, M., Lopes, F., Cummings, C., Springer, C.J., Chesler, L., Jones, C., Bamber, J.C., Yuan, Y., Sinkus, R., Jamin, Y., Robinson, S.P., 2019. Investigating the contribution of collagen to the tumor biomechanical phenotype with noninvasive magnetic resonance elastography. Cancer Research 79(22), 5874-5883. https//doi.org/10.1158/0008-5472.CAN-19-1595

Lorenzen J., Sinkus R., Lorenzen M., Dargatz M., Leussler C., Röschmann P., Adam G., 2002. MR elastography of the breast: preliminary clinical results. Röfo 174(7), 830-834. https//doi.org/10.1055/s-2002-32690

McKnight, A.L., Kugel, J.L., Rossman, P.J., Manduca, A., Hartmann, L.C., Ehman, R.L., 2002. MR elastography of breast cancer: Preliminary results. American Journal of Roentgenology 178(6), 1411-1417. https//doi.org/10.2214/ajr.178.6.1781411

Nicolle, S., Palierne, J.-F., 2010. Dehydration effect on the mechanical behaviour of biological soft tissues: observations on kidney tissues. Journal of the Mechanical Behavior of Biomedical Materials 3, 630-635. https//doi.org/10.1016/j.jmbbm.2010.07.010

Nicolle, S., Palierne, J.-F, 2012. On the efficiency of attachment methods of biological soft tissues in shear experiments. Journal of the Mechanical Behavior of Biomedical Materials 14, 158-162. https//doi.org/10.1016/j.jmbbm.2012.05.002

Nicolle, S., Noguer, L., Palierne, J.-F., 2013. Shear mechanical properties of the porcine pancreas: Experiments and analytical modeling. Journal of the Mechanical Behavior of Biomedical Materials 26, 90-97. https//doi.org/10.1016/j.jmbbm.2013.05.029

Nicolle, S., Decorps, J., Fromy, B., Palierne, J.-F., 2017. New regime in the mechanical behavior of skin: strain-softening occurring before strain-hardening. Journal of the Mechanical Behavior of Biomedical Materials 69, 98-106. https//doi.org/10.1016/j.jmbbm.2016.12.021

Papazoglou, S., Hirsch, S., Braun, J., Sack, I., 2012. Multifrequency inversion in magnetic resonance elastography. Physics in Medicine and Biology 57 (2012) 2329–2346 https//doi.org/10.1088/0031-9155/57/8/2329

Pathmanathan, P., Gavaghan, D.J., Whiteley, J.P., Chapman, S.J., Brady, J.M., 2008. Predicting tumor location by modeling the deformation of the breast. IEEE Transactions on Biomedical Engineering 55(10), 2471-2480. https//doi.org/10.1109/TBME.2008.925714

Pepin, K.M., Ehman, R.L., McGee, K.P., 2015. Magnetic resonance elastography (MRE) in cancer: Technique, Analysis and applications. Progress in Nuclear Magnetic Resonance Spectroscopy 90-91, 32-48. https//doi.org/10.1016/j.pnmrs.2015.06.001

Peyruchaud, O., Winding, B., Pécheur, I., Serre, C.-M., Delmas, P., Clézardin, P., 2001. Early Detection of Bone Metastases in a Murine Model Using Fluorescent Human Breast Cancer Cells: Application to the Use of the Bisphosphonate Zoledronic Acid in the Treatment of Osteolytic Lesions. Journal of Bone and Mineral Research 16(11), 2027-2034. https//doi.org/10.1359/jbmr.2001.16.11.2027

Ramião, N.G., Martins, P.S., Rynkevis, R., Fernandes, A.A., Barroso, M., Santos D.C., 2016. Biomechanical properties of breast tissues, a state-of-the-art review. Biomechanics and Modeling in Mechanobiology 15, 1307-1323. https//doi.org/10.1007/s10237-016-0763-8

Rasband W.S., 1997–2012. ImageJ, U.S. National Institutes of Health, Bethesda, Maryland, USA, https://imagej.nih.gov/ij/.

Reynolds, O., 1886. On the Theory of Lubrication and its Application to Mr BEAUCHAMP TOWER'S Experiments, including an Experimental Determination of the Viscosity of Olive Oil. Proc. Roy. Soc.177, 157-234. https//doi.org/10.1098/rstl.1886.0005

Rieger, M.M., Deem, D.E., 1974. Skin moisturizers. I – Methods for measuring water regain, mechanical properties, and transepidermal moisture loss of stratum corneum. Journal of the Society of Cosmetic Chemists 25, 239-252. https://library.scconline.org/v025n05/1

Riek, K., Klatt, D., Nuzha, H., Mueller, S., Neumann, U., Sack, I., Braun, J., 2011. Wide-range dynamic magnetic resonance elastography. Journal of Biomechanics 44, 1380-1386. https//doi.org/10.1016/j.jbiomech.2010.12.031

Robertson, D., Cook, D., 2014. Unrealistic statistics: How average constitutive coefficients can produce non-physical results. Journal of the Mechanical Behavior of Biomedical Materials 40, 234-239. https://doi.org/10.1016/j.jmbbm.2014.09.006

Sack, I., Beierbach, B., Wuerfel, J., Klatt, D, Hamhaber, U, Papazoglou, S, Martus, P, Braun, J, 2009. The impact of aging and gender on brain viscoelasticity. NeuroImage 46, 652-657. https//doi.org/10.1016/j.neuroimage.2009.02.040

Sack, I., Jöhrens, K., Würfel, J., Braun, J., 2013. Structure-sensitive elastography: on the viscoelastic powerlaw behavior of *in vivo* human tissue in health and disease. Soft Matter 9, 5672-5680. https//doi.org/10.1039/c3sm50552a

Samani, A., Plewes, D., 2004. A method to measure the hyperelastic parameters of ex vivo breast tissue samples. Physics in Medicine and Biology 49, 4395-4405. https//doi.org/10.1088/0031-9155/49/18/014

Samani, A., Zubovits, J., Plewes, D., 2007. Elastic moduli of normal and pathological human breast tissues: A inversion-technique-based investigation of 169 samples. Physics in Medicine & Biology 52(6), 1565-1576. https//doi.org/10.1088/0031-9155/52/6/002

Sarvazyan, A., Hall T.J., Urban, M.W., Fatemi, M., Aglyamov, S.R., Garra, B.S., 2011. An overview of elastography-An emerging branch of medical imaging. Current Medical Imaging Reviews 7, 255-282. https//doi.org/10.2174/157340511798038684

Sauer, F., Oswald, L., Ariza de Schellenberger, A., Tzschätzsch, H., Schrank, F., Fischer, T., Braun, J., Mierke, C.T., Valiullin, R., Sack, I., Käs, J.A., 2019. Collagen networks determine viscoelastic properties of connective tissues yet do not hinder diffusion of the aqueous solvent. Soft Matter 15, 3055-3064. https//doi.org/10.1039/c8sm02264j

Schmidt, K.M., Geissler, E.K., Lang, S.A., 2016. Subcutaneous murine xenograft models: A critical tool for studying human tumor growth and angiogenesis in vivo. Methods in Molecular Biology 1464, 129-137. https//doi.org/10.1007/978-1-4939-3999-2_12

Siegmann, K.C., Xydeas, T., Sinkus, R., Kraemer, B., Vogel, U., Claussen, C.D., 2010. Diagnostic Value of MR Elastography in Addition to Contrast-Enhanced MR Imaging of the Breast-Initial Clinical Results. European Radiology 20, 318-325. https//doi.org/10.1007/s00330-009-1566-4

Sinkus, R., Lorenzen, J., Schrader D., Lorenzen D., Dargatz M., Holz D., 2000. High-resolution tensor MR elastography for breast tumour detection. Physics in Medicine & Biology 45, 1649-1664. https//doi.org/10.1088/0031-9155/45/6/317

Sinkus, R., Tanter, M., Catheline, S., Lorenzen, J., Kuhl, C., Sondermann, E., Fink, M., 2005. Imaging anisotropic and viscous properties of breast tissue by magnetic resonance-elastography. Magnetic Resonance in Medicine 53, 372-387. https//doi.org/10.1002/mrm.20355

Sinkus, R., Siegmann, K., Xydeas, T., Tanter, M., Claussen, C., Fink, M., 2007. MR Elastography of Breast Lesions: Understanding the Solid/Liquid Duality Can Improve the Specificity of Contrast-Enhanced MR Mammography. Magnetic Resonance in Medicine 58:1135–1144. https//doi.org/10.1002/mrm.21404

Tan, K., Cheng, S., Jugé, L., Bilston, L.E., 2015. Characterizing skeletal muscle under large strain using eccentric and Fourier-Transform rheology. Journal of Biomechanics 48:3788-3795. https//doi.org/10.1016/j.jbiomech.2015.08.025

Tanner, C., Degenhard, A., Schnabel, J.A., Castellano-Smith, A.D., Hayes, C., Sonoda, L.I., Leach, M.O., Hose, D.R., Hill, D.L.G., Hawkes, D.J., 2002. Comparison of biomechanical breast models : a case of study. Proceedings of SPIE Volume 4684, Medical Imaging 2002: Image Processing, San Diego, California, United States. https//doi.org/10.1117/12.467155

Tschoegl, N.W., 1989. The phenomenological theory of linear viscoelastic behavior: An introduction. Springer-Verlag Berlin Heidelberg, p 769. https//doi.org/10.1007/978-3-642-73602-5

Umemoto, T., Ueno, E., Matsumara, T., Yamakawa, M., Bando, H., Mitake, T., Shiina, T., 2014. *Ex vivo* and *in vivo* assessment of the non-linearity of elasticity properties of breast tissues for quantitative strain elastography. Ultrasound in Medicine & Biology 40, 1755-1768. https//doi.org/10.1016/j.ultrasmedbio.2014.02.005

Wellman, P.S., Howe, R.D., Dalton, E., Kern, K.A., 1999. Breast tissue stiffness in compression is correlated to histological diagnosis. Harvard BioRobotics Laboratory Technical Report, 1-15.

Wells, P.N.T., Liang, H.-D., 2011. Medical ultrasound: imaging of soft tissue strain and elasticity. Journal of the Royal Society Interface 8(64), 1521-1549. https//doi.org/10.1098/rsif.2011.0054

Yeung, J., Jugé, L., Hatt, A., Bilston, L.E., 2019. Paediatric brain tissue properties measured with magnetic resonance elastography. Biomechanics and Modeling in Mechanobiology 18, 1497-1505. https//doi.org/10.1007/s10237-019-01157-x

Xydeas, T., Siegmann, K., Sinkus, R., Krainick-Strobel, U., Miller, S., Claussen, C.D., 2005. Magnetic resonance elastography of the breast: Correlation of signal intensity data with viscoelastic properties. Investigative Radiology 40(7), 412-420. https//doi.org/10.1097/01.rli.0000166940.72971.4a

Highlights

- The frequency dependence of moduli discriminates tumors from healthy tissues
- Tumors are more elastic than healthy tissues
- The spring-pot model describes the linear viscoelastic behavior of soft tissues
- Multi-frequency measurements could improve diagnosis by MR elastography

Declaration of interests

☒ The authors declare that they have no known competing financial interests or personal relationships that could have appeared to influence the work reported in this paper.

☐ The authors declare the following financial interests/personal relationships which may be considered as potential competing interests: